Available online at www.sciencedirect.com
ScienceDirect
Trans. Nonferrous Met. Soc. China 31(2021) 1758−1765
Transactions of Nonferrous Metals Society of China
www.tnmsc.cn

# Rate-dependent inhomogeneous creep behavior in metallic glasses

Hong WU[1,2,3], Feng XU[1,4], Jun-ye REN[1], Xiao-dong LAN[1], Yong YIN[1],
Lu-xin LIANG[1], Min SONG[1], Yong LIU[1], Jia LI[5], Qing-xiang LI[2], Wei-dong HUANG[3]

1. State Key Laboratory of Powder Metallurgy, Central South University, Changsha 410083, China;
2. Shenzhen Zhongjin Lingnan Nonfemet Co., Ltd., Shenzhen 518040, China;
3. School of Materials Science and Engineering, Northwestern Polytechnical University, Xi'an 710072, China;
4. Farsoon Technologies, Changsha 410205, China;
5. State Key Laboratory of Advanced Design and Manufacturing for Vehicle Body,
Hunan University, Changsha 410082, China

Received 5 July 2020; accepted 26 December 2020

**Abstract:** Creep deformation can be classified as homogeneous flow and inhomogeneous flow in bulk metallic glass (BMG). In order to understand the conversion conditions of the two types of creep deformation, the effect of loading rate on the creep behavior of a $Ti_{40}Zr_{10}Cu_{47}Sn_3$ (at.%) BMG at ambient temperature was investigated using nanoindentation and molecular dynamic simulation. Results indicate that at low loading rates, many serrations appear in loading stage, leading to inhomogeneous serrated flow in the creep stage. When the loading rate is high enough, the creep deformation tends to be homogeneous. The related mechanism responsible for the rate-dependent creep behavior is attributed to the number of pre-existing major shear bands which is influenced significantly by the loading rate.
**Key words:** metallic glasses; nanoindentation; loading rate; inhomogeneous creep; shear band

## 1 Introduction

Since bulk metallic glasses (BMGs) exhibit extremely high strength and large elastic strain limit at room temperature, they are generally considered as potential structural materials [1−3]. However, the poor plasticity at room temperature restricts their applications, and thus significant efforts have been made to understand the plastic deformation behaviors of BMGs [4]. After years of research, it is well accepted that the plastic deformation of BMGs is related to the local rearrangement of atoms, which possess much larger displacement than the surrounding atoms, called shear transformation zones (STZs) [5−7]. The activation of STZs in stressed BMGs could form shear bands which significantly influence the plastic deformation [8]. The plastic deformation mode of BMGs can basically be classified into two types, i.e. homogeneous flow and inhomogeneous flow. When the stress is relatively low and the temperature is high (above and near the glass transition temperature $T_g$), homogeneous flow occurs, where independent STZs contribute to the strain [5,9]. Oppositely, inhomogeneous deformation usually occurs at high stress and low temperature in a few localized narrow shear bands, which are promoted by free volume and thermal softening induced by atomic rearrangements in coupling with the STZs [5,10−12]. Inhomogeneous flow eventually results in strain softening and macroscopically catastrophic failure. Flow serration, associated with inhomogeneous flow, is a commonly observed

**Corresponding author:** Hong WU, E-mail: wuhong927@126.com, hwucsu@csu.edu.cn; Lu-xin LIANG, E-mail: liang_luxin@163.com; Jia LI, E-mail: lijia123@hnu.edu.cn
DOI: 10.1016/S1003-6326(21)65614-5

phenomenon both in uniaxial compression [13] and sharp indentation test of BMGs [14].

Creep is a time-dependent plastic deformation behavior. The creep behaviors of BMGs have attracted much attention due to their unique atomic structure [15]. Similar to the quasi-static plastic deformation such as uniaxial compression, creep can be identified as homogeneous creep or inhomogeneous creep, in which flow serrations were also reported [16,17]. For example, YOO et al [18] investigated the creep behavior of two CuZr BMGs and found that the creep is homogeneous and the amount of creep deformation is sensitive to the indentation strain, which can be adjusted by the applied peak load. LI et al [16] pointed out that the inhomogeneous creep occurs in the specific regions (soft regions) of CuZrAlAg BMG during nanoindentation, and proposed that local structural diversity may be a key factor in determination of creep behavior. However, the conversion condition between homogeneous creep deformation and inhomogeneous creep deformation is still not clear. The objective of this work is to explore the conversion conditions of different types of creep behavior of a TiCu-based BMG.

Further, it is well known that strain rate plays a significant role in affecting the microstructure and mechanical properties of BMGs [19−21]. For instance, strain rate extensively affects the yielding strength in tension and compression tests [22], the serrated flow in compression tests [23] and nanoindentation tests [14], and the creep stress component in nanoindentation creep tests [24]. SCHUH and NIEH [14] found that the plastic deformation of a Pd−30Cu−10Ni−20P BMG generally corresponds to individual load serrations at low indentation rates. Oppositely, if indentation rate is high enough, none of the measured plasticity can be attributed to load serrations. The effect, however, of strain rate on the serrated flow of creep during the nanoindentation process is still unclear up to now. Since creep occurs immediately after the loading stage, the strain rate at loading stage can affirmatively modify the local microstructures of deformation regions, subsequently affecting the creep behaviors.

Nanoindentation is widely used in investigating the mechanical response of various materials due to its high accuracy in well-controlled conditions [25]. In this work, nanoindentation tests and molecular dynamic simulations were used to study the different types of creep behavior at different rates. The related mechanisms were discussed in detail.

## 2 Experimental

### 2.1 Materials and methods

The master alloy with a nominal composition of $Ti_{40}Zr_{10}Cu_{47}Sn_3$ (at.%) was fabricated through arc melting a mixture of Ti (99.8%), Zr (99.8%), Cu (99.99%), and Sn (99.99%) in a high-purity argon atmosphere. The ingot was remelted four times to ensure compositional homogeneity, and then suction cast into specimens with diameter of 2 mm and length of 60 mm in water-cooled copper molds. The glassy structure of the alloys was examined using a Rigaku D/max-2550VB X-ray diffractometer (XRD) and an FEI Tecnai G2 F20 transmission electron microscope (TEM). The thermodynamic behavior was characterized using an SDT Q600 differential scanning calorimeter (DSC), by heating from room temperature to 700 °C at a heating rate of 20 °C/min under flowing argon. The surfaces of specimens were mechanically polished before being subjected to nanoindentation tests using a nanoindenter (UNHT) with a Berkovich diamond tip at room temperature. Small errors such as noise and thermal drift can be eliminated in real time. The nanoindentation tests were performed in a load-control mode at different loading rates ($dP/dt$ of 0.05, 0.1, 0.5, 1 and 5 mN/s). After loading, the indenter was held at a maximum load ($P_{max}$ of 30 mN) for 1000 s. A data acquisition of 10 points/s was applied to recording the displacement–time curves and capture possible serrated flow. Nanoindentation tests at each loading rate were performed at least five times to ensure repeatability.

### 2.2 Simulation

A molecular dynamics model in Fig. 1 containing 195200 atoms, with a size of 144 Å × 144 Å × 253 Å was constructed to investigate the nanoindentation process. The TiZrCu BMG model was obtained by randomly replacing atoms in Ti crystal to meet the specific molar fraction (40% Ti, 10% Zr, 50% Cu) at first, and then accompanied by subsequent melting and quenching [26]. The diamond spherical indenter with a diameter of 20 Å

(containing 34850 atoms) was regarded as a rigid structure. Periodic boundary conditions were used in the *X* and *Y* directions, and free boundary condition was applied in the *Z* direction. The atoms in the model were classified into 3 categories. Boundary atoms with a thickness of 10 Å were fixed at the bottom. Thermostat atoms with a thickness of 10 Å were set next to boundary atoms. The rest of the atoms were set as Newtonian atoms [27] which meet the Newton's second law.

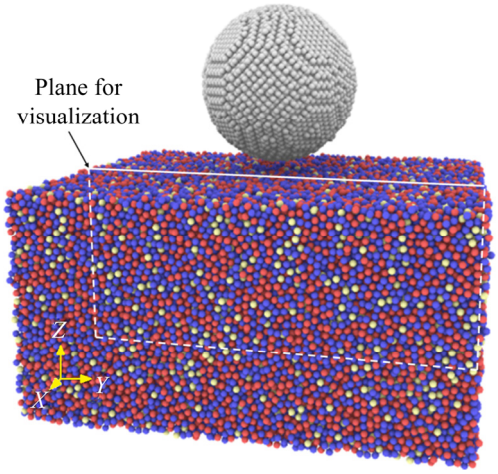


**Fig. 1** TiZrCu BMG model used in simulation

The initial temperature of the TiZrCu BMG sample was set as 20 °C. The temperature was kept at the beginning temperature by readjusting the thermostat set. The micro-canonical (NVE) ensemble was adopted during indentation. Large-scale atomic/molecular massively parallel simulator (LAMMPS) was applied in the present study, and all of the simulations were performed with the time step of 1 fs [28]. The embedded atom method (EAM) potential was employed for the atomic interaction of TiZrCu BMG, while the interaction between TiZrCu BMG and tool used Morse potential [27,29]. The visualization was conducted with the open source software OVITO [30]. To obtain the comparable elastic modulus between simulation and experiment, reduced elastic modulus was used to characterize the elastic property of the model, which was obtained according to the work of OLIVER and PHARR [25]. Based on the Hertz theory, the force can be expressed as $F=4/3r^{1/2}E^{*}h^{3/2}$, where $r$ represents the indenter radius, $h$ represents the depth of indentation, and $E^{*}$ represents the reduced elastic modulus which can be calculated by $1/E^{*}=(1-\nu^{2})/E+(1-\nu')E'$, where $E$ and $\nu$ are the elastic modulus and Poisson ratio of the substrate, respectively, and $E'$ and $\nu'$ are the elastic modulus and Poisson ratio of the indenter, respectively. Here, $\nu$ is set as 0.36 [31], and $E^{*}$ of the TiZrCu BMGs is 61 GPa.

As the simulated indentation test started, the indenter moved in the *Z* direction at a constant speed rather than a fixed loading rate to simplify the simulation process. The force of the indenter was then recorded automatically and the shear strain in the model was calculated. The plane for visualization was parallel to the *YZ* plane and coincided with the center of the model (Fig. 1). Three indentation speeds (1, 5 and 50 m/s) were used to study the difference in shear deformation behavior.

## 3 Results

### 3.1 Amorphous properties

Figure 2 shows the XRD pattern and DSC curve of the as-cast $Ti_{40}Zr_{10}Cu_{47}Sn_3$ rod. It mainly consists of a broad peak and there are no visible

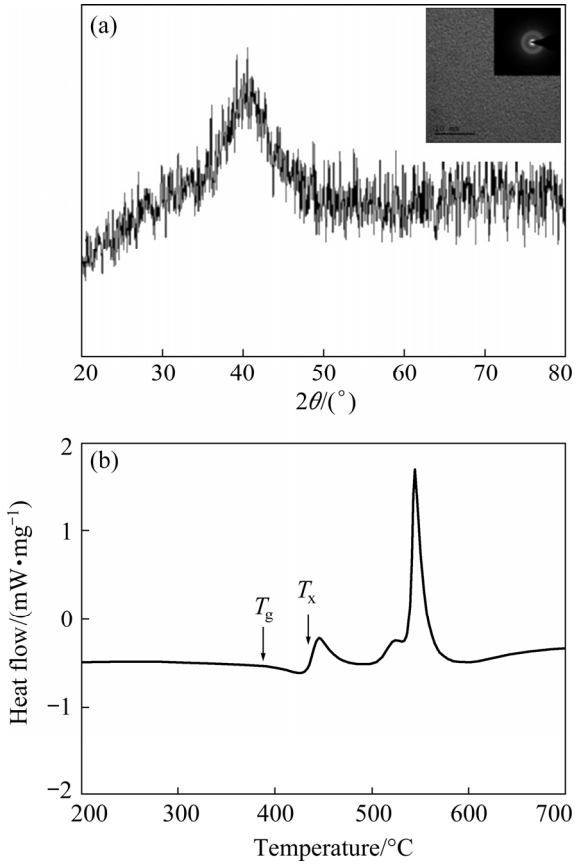


**Fig. 2** XRD pattern and corresponding electron diffraction pattern with high-resolution TEM image (a), and DSC curve (b) of as-cast $Ti_{40}Zr_{10}Cu_{47}Sn_3$ BMG

sharp Bragg peaks corresponding to the crystalline phases (Fig. 2(a)). This indicates the almost fully amorphous structure of the as-cast alloy. The mazelike pattern of TEM image and selected-area electron diffraction (SAED) pattern inset in Fig. 2(a) imply that no phase separation occurred during casting, further demonstrating the amorphous nature of the specimen. As indexed in Fig. 2(b), the glass transition temperature ($T_g$) and the onset crystallization temperature ($T_x$) of the as-cast alloy are 383 and 441 °C, respectively. Therefore, the super cooled liquid region, $\Delta T_x$ ($\Delta T_x=T_x-T_g$) can be determined as 58 °C.

### 3.2 Creep behaviors

To investigate the loading rate sensitivity of the creep deformation, nanoindentation tests were conducted at different loading rates. Displacement–time curves for as-cast sample at different loading rates are shown in Fig. 3. The demarcation points between loading region and creep region on the curves were shifted to the same time for better comparison. Serrated flows, regarded as inhomogeneous deformation, are observed on the curves in loading region (Fig. 3(b)). This obviously shows that the higher the loading rate is, the more the serrations appeared at the loading stage.

Unlike the tests conducted at low loading rates, no distinct serration was found on the displacement–time curve in the creep region at a loading rate of 5.00 mN/s (Fig. 3(b)), indicating the occurrence of homogeneous flow. Similarly, the number of serrations at the creep stage is significantly dependent on the loading rate performed before creep.

To quantify the effect of shear banding on the creep behavior, the size of each serration, the total displacement and the number of serrations both at loading and creep stages were counted and calculated statistically. Figure 4(a) illustrates the distribution of the serrations at the loading stage and the creep stage with different loading rates. The calculated total number and displacement of the serrations are shown in Fig. 4(b). It is obvious that the number and displacement of the serrations

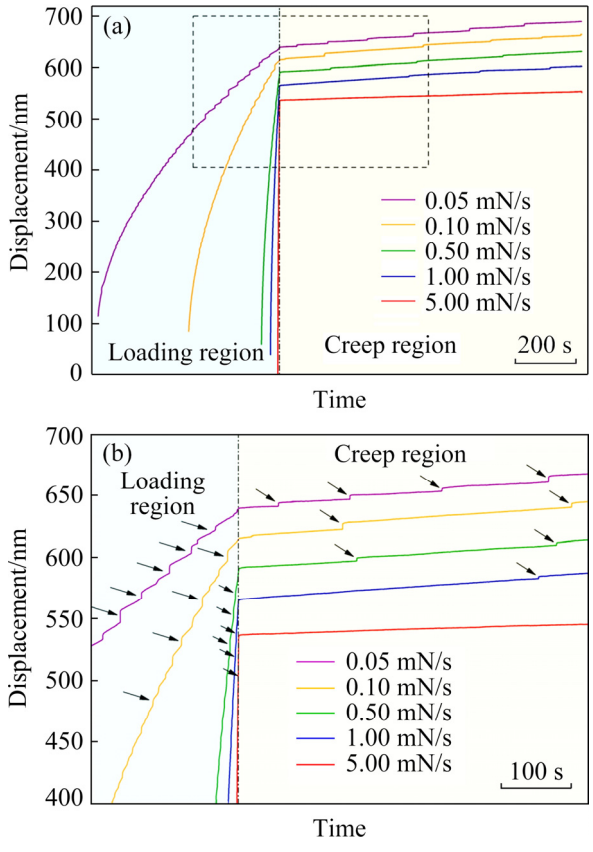


**Fig. 3** Displacement–time curves of nanoindentation tests at different loading rates (a) and enlarged view (b) of dashed rectangle in (a)

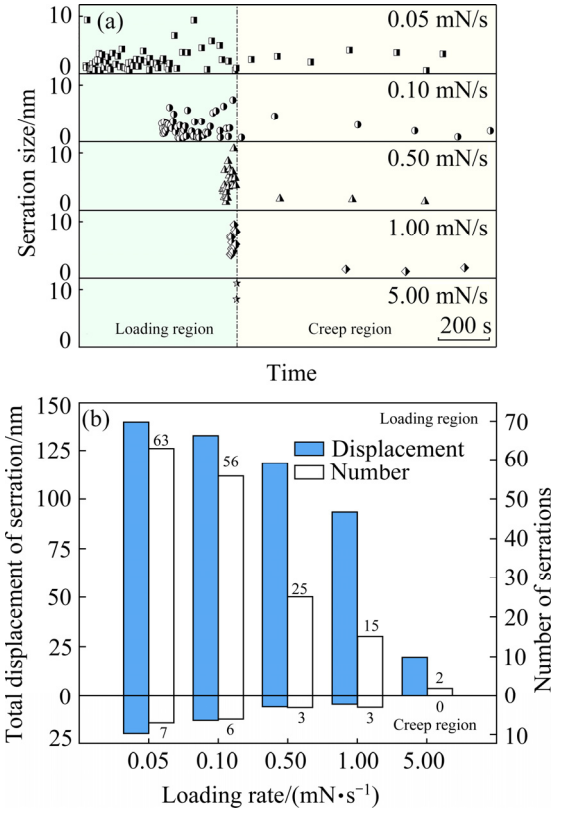


**Fig. 4** Distribution of serrations in both loading region and creep region of displacement–time curves with different loading rates (a), and total displacement and number of serrations statistically calculated from loading region and creep region (b)

decrease remarkably with the up-regulated loading rate in both loading region and creep region.

### 3.3 Molecular dynamics simulation

To further illustrate the shear banding events evolution during loading, a molecular dynamics model was introduced. The elastic modulus ($E$) of the TiZrCu model with the indentation depth of 2.5 nm (Fig. 5) is 53 GPa. This is approximately consistent with the previous study [32], and thus ensures the validity of the simulations.

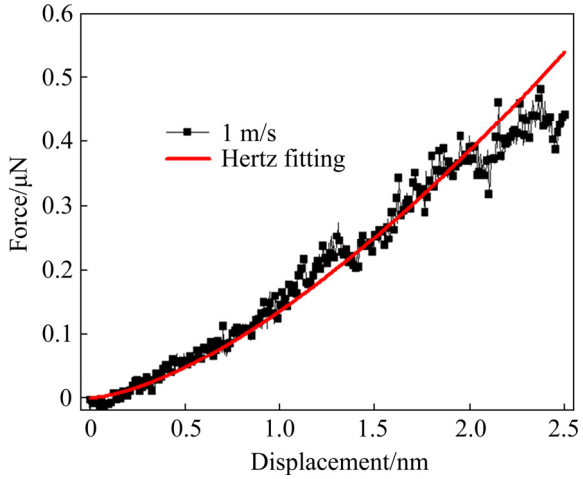


**Fig. 5** Force−displacement curve of simulation process

Force–displacement curves simulated at various indentation speeds are presented in Fig. 6(a). Serrations caused by fluctuation of indentation force can be observed on all simulated curves. The Hertz fitting curve stimulated at lower indentation speeds exhibits severer fluctuations. Snapshots of the strain distribution at different indentation speeds are shown in Fig. 6. The strain in the small zone beneath the high strain region located around the indenter is inhomogeneous, in which assembly of large-strain atoms is surrounded by small-strain atoms. These are described as shear strain zones (SSZs), marked as yellow ring in Figs. 6(b−d). A number of SSZs are detected in the model stimulated at 1 m/s, while only a few SSZs can be found in the model stimulated at 50 m/s. It is worth noting that the uniformity of strain is better in the model under high indentation speeds than low indentation speeds.

## 4 Discussion

The initiation and propagation of shear bands are regarded as slip avalanches of STZs [33]. A number of STZs assembled cooperatively to form a shear band, in which the highly localized strain

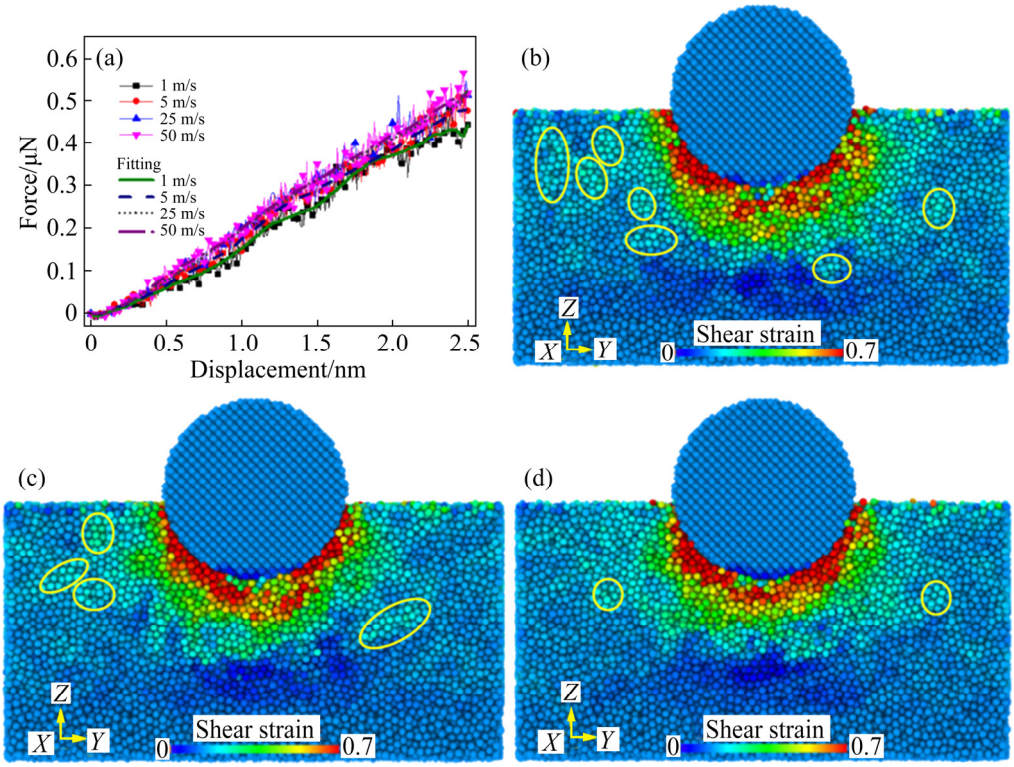


**Fig. 6** Force–displacement curves and Hertz fitting curves at different indentation speeds (a), strain distributions of TiZrCu BMG using molecular dynamic simulation at different indentation speeds of 1 m/s (b), 5 m/s (c), and 50 m/s (d)

accumulated via sustained uniform shearing [34]. SONG et al [35] reported a one-to-one correspondence between the serration on the load−displacement curve and the sliding on the BMG sample through in situ compression tests. The single shear along a principal shear plane is believed to be the cause of serrations when strain rate is relatively low [35]. Accordingly, in the present study, the serrations on the displacement−time curve can be considered as the accumulation of displacement via localized deformation, which varies significantly between the tests performed at different loading rates.

### 4.1 Loading stage

At the loading stage, STZs in BMGs nucleate and then shear bands initiate when the load and deformation increase. The initiation and propagation of shear bands significantly depend on the strain rate [19,22,23]. At a low loading rate, an agminated shear zone formed via assembly of STZs at first and then large displacements accumulated in it to relax the loading stress, which can also be considered as large slip events [33]. This led to the occurrence of highly localized strain, i.e. shear banding, which appeared as evident serrations on the curve of loading region [14,35]. In the present study, a large number of serrations can be observed on the curves at low loading speeds, indicating the existence of shear bands, where highly localized strain accumulated (Fig. 4), which are regarded as dominant shear bands. Similarly, the large stress drop can also be observed on the curves simulated at low indentation speeds (Fig. 6(a)). More coupled SSZs denote the high probability for the formation of shear bands either (Fig. 6(b)). Furthermore, shear banding events in deformed BMGs often increase the free volume and lead to the strain softening [4,5,9,10], which could sequentially strengthen the inhomogeneous flow at both loading and creep stages [16]. As the loading rate is increased, the relaxation velocity of slip along shear bands is not enough to adapt the rapidly increased strain [36]. Simultaneously, ultrafine shear bands may nucleate instead of the dominant shear bands. Although few large serrations are observed both on experimental and simulation curves at high loading rates (Fig. 3, Fig. 6(a)), extremely small serrations related to ultrafine shear bands exactly do exist [37]. It is difficult to characterize these fine serrations due to the limited resolution of the indentation equipment [38]. However, these can be observed on the simulated curves (Fig. 6(a)). When the loading rate is sufficiently high, the assembly velocity of STZs may be not enough to adapt the high strain rate. This gives rise to the accommodation of independent STZs (sporadic SSZs in Fig. 6(d)), hence exhibiting homogeneous flow. QIAO et al [23] reported a similar rate-dependent phenomenon in compression tests, and suggested that the occurrence of inhomogeneous flow was strongly related to the critical strain rate.

### 4.2 Creep stage

Shear bands accumulated highly-localized strain generated at the loading stage increase the free volume of plastically deformed regions [5,9,39], in which STZs sequentially assemble and form new shear bands under the constant stress at the creep stage [18]. In addition, some of the pre-existed dominant shear bands are likely to be reactivated and propagate continuously [40]. In the present study, the number of pre-existed dominant shear bands immediately before creep is sufficient for the BMG tested at a low loading rate (Fig. 4), which further triggers the occurrence of multi-serrations at the creep stage. At high loading rates, in contrast, the deformed specimen contains few dominant shear bands immediately before creep and the initiation of new shear bands and/or propagation of pre-existing shear bands are inhibited. Since the strain rate of creep stage is much lower than that of loading stage, the propagation of fine shear bands is not able to form dominant shear bands at the creep stage. Consequently, these give rise to homogeneous flow without observable serrations on the curve (Fig. 3).

## 5 Conclusions

(1) The more the serrations appearing at the loading stage, the more the significant inhomogeneous flow (serrations) that occurs at the creep stage. The key factor that determines the creep behavior is the number of the dominant shear bands pre-existed.

(2) At low loading rate, local strain is accommodated by dominant shear banding events, leading to serrated flow at both loading and creep

stages. As the loading rate increases, serrated flow and dominant shear banding events affect the serrations and the evolution of shear bands at the creep stage. When the loading rate reaches 5.00 mN/s, the homogeneous creep occurs.

## Acknowledgments

This work was supported by the National Key Research and Development Program of China (No. 2016YFB1100103), the National Natural Science Foundation of China (No. 51771233), Key Research and Development Program of Hunan Province, China (No. 2016JC2003), China Post-doctoral Science Foundation (No. 2018M633164), and Fundamental Research Funds for the Central Universities of Central South University, China (Nos. 2018ZZTS127, CX20190190, 2019ZZTS-134).

## References

[1] HAYS C C, KIM C P, JOHNSON W L. Microstructure controlled shear band pattern formation and enhanced plasticity of bulk metallic glasses containing in situ formed ductile phase dendrite dispersions [J]. Physical Review Letters, 2000, 84: 2901−2904.

[2] WANG Wei-hua. Roles of minor additions in formation and properties of bulk metallic glasses [J]. Progress in Materials Science, 2007, 52: 540−596.

[3] LAN Xiao-dong, WU Hong, LIU Yong, ZHANG Wei-dong, LI Rui-di, CHEN Shi-qi, ZAI Xiong-fei, HU Te. Microstructures and tribological properties of laser cladded Ti-based metallic glass composite coatings [J]. Materials Characterization, 2016, 120: 82−89.

[4] TREXLER M M, THADHANI N N. Mechanical properties of bulk metallic glasses [J]. Progress in Materials Science, 2010, 55: 759−839.

[5] ARGON A S. Plastic deformation in metallic glasses [J]. Acta Metalurgica, 1979, 27: 47−58.

[6] JIANG S S, GAN K F, HUANG Y J, XUE P, NING Z L, SUN J F, NGAN A H W. Stochastic deformation and shear transformation zones of the glassy matrix in CuZr-based metallic-glass composites [J]. International Journal of Plasticity, 2020, 125: 52−62.

[7] LEI T J, DACOSTA L R, LIU M, SHEN J, SUN Y H, WANG W H, ATZMON M. Composition dependence of metallic glass plasticity and its prediction from anelastic relaxation−A shear transformation zone analysis [J]. Acta Materialia, 2020, 195: 81−86.

[8] PEREPEZKO J H, IMHOFF S D, CHEN Ming-wei, WANG Jun-qiang, GONZALEZ S. Nucleation of shear bands in amorphous alloys [J]. Proceedings of the National Academy of Sciences of the United States of America, 2014, 111: 3938−3942.

[9] SPAEPEN F. Homogeneous flow of metallic glasses: A free volume perspective [J]. Scripta Materialia, 2006, 54: 363−367.

[10] SPAEPEN F. A microscopic mechanism for steady state inhomogeneous flow in metallic glasses [J]. Acta Metallurgica, 1977, 25: 407−415.

[11] HOMER E R, SCHUH C A. Mesoscale modeling of amorphous metals by shear transformation zone dynamics [J]. Acta Materialia, 2009, 57: 2823−2833.

[12] WU Hong, LIU Yong, LI Kai-yang, ZHAO Zhong-wei. Casting effect on compressive brittleness of bulk metallic glass [J]. Transactions of Nonferrous Metals Society of China, 2014, 24: 385−392.

[13] LIU L F, DAI L H, BAI Y L, WEI B C, YU G S. Strain rate-dependent compressive deformation behavior of Nd-based bulk metallic glass [J]. Intermetallics, 2005, 13: 827−832.

[14] SCHUH C A, NIEH T G. A nanoindentation study of serrated flow in bulk metallic glasses [J]. Acta Materialia, 2003, 51: 87−99.

[15] LI Chun-yan, LI Xin-ling, ZHAO Zhen-xiang, ZHU Fu-ping, KOU Sheng-zhong, ZHAO Yan-chun. Effect of peak loads and cooling rates on creep behavior of Zr-based bulk metallic glass [J]. Journal of Non-Crystalline Solids, 2019, 522: 119596.

[16] LI Fu-cheng, XIE Ya, GU Ji, SONG Min, NI Song, GUO Sheng-feng, LIAO Xiao-zhou. Inhomogeneous creep deformation in metallic glasses [J]. Materials Science and Engineering A, 2015, 648: 57−60.

[17] YU P F, FENG S D, XU G S, GUO X L, WANG Y Y, ZHAO W, QI L, LI G, LIAW P K, LIU R P. Room-temperature creep resistance of Co-based metallic glasses [J]. Scripta Materialia, 2014, 90−91: 45−48.

[18] YOO B G, KIM K S, OH J H, RAMAMURTY U, JANG J. Room temperature creep in amorphous alloys: Influence of initial strain and free volume [J]. Scripta Materialia, 2010, 63: 1205−1208.

[19] NIEH T G, SCHUH C, WADSWORTH J, LI Yi. Strain rate-dependent deformation in bulk metallic glasses [J]. Intermetallics, 2002, 10: 1177−1182.

[20] XU Yuan-li, SHI Bo. Effects of strain and strain rate on the evolution of shear bands for room temperature rolled Pd 40 Ni 40 P 20 bulk metallic glass [J]. Journal of Non-Crystalline Solids, 2018, 485: 74−81.

[21] KOZIEŁ T, PAJOR K, CIOS G, BAŁA P. Effect of strain rate and crystalline inclusions on mechanical properties of bulk glassy and partially crystallized Zr52.5Cu17.9Ni14.6Al10Ti5 alloy [J]. Transactions of Nonferrous Metals Society of China, 2019, 29: 1036−1045.

[22] LI M C, JIANG M Q, YANG S, JIANG F, HE L, SUN J. Effect of strain rate on yielding strength of a Zr-based bulk metallic glass [J]. Materials Science and Engineering A, 2017, 680: 21−26.

[23] QIAO J W, ZHANG Y, LIAW P K. Serrated flow kinetics in a Zr-based bulk metallic glass [J]. Intermetallics, 2010, 18: 2057−2064.

[24] HUANG Y J, SHEN J, CHIU Y L, CHEN J J J, SUN J F. Indentation creep of an Fe-based bulk metallic glass [J]. Intermetallics, 2009, 17: 190−194.

[25] OLIVER W C, PHARR G M. An improved technique for determining hardness and elastic modulus using load and

displacement sensing indentation experiments [J]. Journal of Materials Research, 1992, 7: 1564−1583.

[26] ZHOU H F, ZHONG C, CAO Q P, QU S X, WANG X D. Non-localized deformation in metallic alloys with amorphous structure [J]. Acta Materialia, 2014, 68: 32−41.

[27] LI Jia, GUO Jia-wen, LUO Hao, FANG Qi-hong, WU Hong, ZHANG Liang-chi, LIU You-wen. Study of nanoindentation mechanical response of nanocrystalline structures using molecular dynamics simulations [J]. Applied Surface Science, 2016, 364: 190−200.

[28] STADLER J, MIKULLA R, TREBIN H R. IMD: A software package for molecular dynamics studies on parallel computers [J]. International Journal of Modern Physics C, 1997, 8: 1131−1140.

[29] ZHANG Jun-jie, BEGAU C, GENG Lin, HARTMAIER A. Atomistic investigation of wear mechanisms of a copper bi-crystal [J]. Wear, 2015, 332−333: 941−948.

[30] STUKOWSKI A. Visualization and analysis of atomistic simulation data with OVITO—the open visualization tool [J]. Modelling and Simulation in Materials Science and Engineering, 2010, 18: 015012.

[31] YU Peng, BAI H Y. Poisson's ratio and plasticity in CuZrAl bulk metallic glasses [J]. Materials Science and Engineering A, 2008, 485: 1−4.

[32] WU Hong, LIANG Lu-xin, LAN Xiao-dong, YIN Yong, SONG Min, LI Rui-di, LIU Yong, YANG Hai-ou, LIU Ling, CAI An-hui, LI Qing-xiang, HUANG Wei-dong. Tribological and biological behaviors of laser cladded Ti-based metallic glass composite coatings [J]. Applied Surface Science, 2020, 507: 145104.

[33] ANTONAGLIA J, WRIGHT W J, GU X, BYER R R, HUFNAGEL T C, LEBLANC M, UHL J T, DAHMEN K A. Bulk metallic glasses deform via slip avalanches [J]. Phys Rev Lett, 2014, 112: 155501.

[34] PACKARD C E, SCHUH C A. Initiation of shear bands near a stress concentration in metallic glass [J]. Acta Materialia, 2007, 55: 5348−5358.

[35] SONG S X, BEI H, WADSWORTH J, NIEH T G. Flow serration in a Zr-based bulk metallic glass in compression at low strain rates [J]. Intermetallics, 2008, 16: 813−818.

[36] XU Fu, ZENG Nan, CHENG Ke-xin, WANG Xin, LONG Shi-guo, DING Yan-huai, YANG Cai-qian. A study of the nanoindentation creep behavior of (La0.5Ce0.5)65Al10Co25 metallic glass based on fractional differential rheological model [J]. Journal of Non-Crystalline Solids, 2018, 490: 50−60.

[37] GREER A L, CASTELLERO A, MADGE S V, WALKER I T, WILDE J R. Nanoindentation studies of shear banding in fully amorphous and partially devitrified metallic alloys [J]. Materials Science and Engineering A, 2004, 375: 1182−1185.

[38] JANGA J, YOO B G, KIM J Y. Rate-dependent inhomogeneous-to-homogeneous transition of plastic flows during nanoindentation of bulk metallic glasses: Fact or artifact [J]. Applied Physics Letters, 2007, 90: 211906.

[39] JIANG S S, GAN K F, HUANG Y J, XUE P, NING Z L, SUN J F, NGAN A H W. Stochastic deformation and shear transformation zones of the glassy matrix in CuZr-based metallic-glass composites [J]. International Journal of Plasticity, 2020, 125: 52-62.

[40] CHEN C Q, PEI Y T, de HOSSON J T M. Effects of size on the mechanical response of metallic glasses investigated through in situ TEM bending and compression experiments [J]. Acta Materialia, 2010, 58: 189−200.

# 金属玻璃中取决于加载速率的非均匀蠕变行为

吴 宏[1,2,3]，徐 峰[1,4]，任俊业[1]，兰小东[1]，殷 勇[1]，
梁陆新[1]，宋 昡[1]，刘 咏[1]，李 甲[5]，李清湘[2]，黄卫东[3]

1. 中南大学 粉末冶金国家重点实验室，长沙 410083；
2. 深圳市中金岭南有色金属股份有限公司，深圳 518040；
3. 西北工业大学 材料科学与工程学院，西安 710072；
4. 湖南华曙高科技有限责任公司，长沙 410205；
5. 湖南大学 汽车车身先进设计制造国家重点实验室，长沙 410082

**摘 要**：大块金属玻璃中的蠕变变形可分为均匀流动和非均匀流动。为了理解两种蠕变变形的转化条件，使用纳米压痕试验和分子动力学模拟研究加载速率对 $Ti_{40}Zr_{10}Cu_{47}Sn_3$ (摩尔分数，%)大块金属玻璃室温蠕变行为的影响。结果发现，在低加载速率下，加载阶段出现很多的锯齿流动，导致蠕变阶段出现非均匀的锯齿流动；而当加载速率足够高时，蠕变变形趋向于均匀流动。详细讨论与速率相关的蠕变行为的相关机制，发现关键因素是预先存在的主要剪切带的数量，该数量受加载速率的影响较大。

**关键词**：金属玻璃；纳米压痕；加载速率；非均匀蠕变；剪切带

**(Edited by Xiang-qun LI)**